Nanoscale Control of an Interfacial Metal-Insulator Transition at Room Temperature

C. Cen[1], S. Thiel[2], G. Hammerl[2], C. W. Schneider[2], K. E. Andersen[3], C. S. Hellberg[3], J. Mannhart[2], J. Levy[1*]

[1]*Department of Physics and Astronomy, University of Pittsburgh, 3941 O'Hara St., Pittsburgh, PA 15260, USA.*

[2]*Experimental Physics VI, Center for Electronic Correlations and Magnetism, Institute of Physics, University of Augsburg, D-86135, Augsburg, Germany.*

[3]*Center for Computational Materials Science, Naval Research Laboratory, Washington, DC 20375, USA.*

Experimental[1-6] and theoretical[7,8] investigations have demonstrated that a quasi-two-dimensional electron gas (q-2DEG) can form at the interface between two insulators: non-polar $SrTiO_3$ and polar $LaTiO_3$[1], $LaAlO_3$[2,3,5] or $LaVO_3$ [6]. Electronically, the situation is analogous to the q-2DEGs formed in semiconductor heterostructures by modulation doping. $LaAlO_3/SrTiO_3$ heterostructures have been shown recently[9] to exhibit a hysteretic electric field-induced metal-insulator quantum phase transition for $LaAlO_3$ thicknesses of 3 unit cells (uc). Here we report the creation and erasure of nanoscale conducting regions at the interface between two insulating oxides, $LaAlO_3$ and $SrTiO_3$. Using voltages applied by a conducting atomic force microscope (AFM) probe, the buried $LaAlO_3/SrTiO_3$ interface is locally and reversibly switched between insulating and conducting states. Persistent field effects are observed using the AFM probe as a gate.

Patterning of conducting lines with widths ~3 nm, as well as arrays of conducting islands with densities >10^{14} in^2, are demonstrated. The patterned structures are stable for >24 hours at room temperature.

The success of semiconductors as technological materials is based on three important features: (1) their electrical conductivity can be tuned over a wide range, either by doping or through electric field effects; (2) insulating layers (i.e., SiO_2) can be formed readily, allowing field effect devices to be fabricated; (3) devices can be scaled to nanoscale dimensions. Oxide materials combine many of the important electronic properties of semiconductors[9,10] with additional emergent phenomena, such as interfacial superconductivity[11], strain-driven ferroelectricity[12], interfacial ferromagnetism[13] and colossal magnetoresistance[14].

The discovery of metallic and superconducting interfaces between insulating oxides has led to many subsequent investigations about the origin of this effect, and in particular the role played by oxygen vacancies[15,16]. In samples that are heated to ~800°C in high vacuum (order of 10^{-6} mbar), oxygen defects are created in the $SrTiO_3$ substrates which *n*-dope the material, regardless of the presence of a $LaAlO_3$ layer[17-20]. For samples grown under oxygen pressures $\geq 10^{-5}$ mbar, (as in the experiments described here), the interfacial conductance is dominated by the potential profile generated between the $SrTiO_3/LaAlO_3$ interface and the top $LaAlO_3$ surface. Thiel et al. found recently that for samples with 3 uc $LaAlO_3$, a bistable metal-insulator transition can be tuned with an voltage applied between the $LaAlO_3/SrTiO_3$ interface and the bottom $SrTiO_3$ substrate[9], suggesting a role played by both the polar discontinuity and residual oxygen vacancies in the $SrTiO_3$.

While oxides provide a wealth of opportunities for probing the rich physics of correlated electronic systems, for technological applications it is essential to scale device concepts to nanoscale dimensions. Here we present a technique which can dynamically define at room temperature nanoscale conducting structures at the interface of two insulating oxides, $LaAlO_3$ and $SrTiO_3$, through reversible control of a localized metal-insulator transition. Both isolated and continuous conducting features with length scales well below 5 nm are demonstrated. Strong nonlinear electric field effects are also observed. We suggest a possible theoretical explanation for this behaviour in terms of the creation of oxygen vacancies in the topmost $LaAlO_3$ surface.

The material system investigated here consists of 3 uc of $LaAlO_3$, grown at 770°C in an O_2 pressure of 6×10^{-5} mbar by pulsed laser deposition on a TiO_2-terminated insulating $SrTiO_3$ substrate[9]. The samples were cooled in 400 mbar of O_2 with a 1 hour oxidation step at 600°C. Several samples were prepared under identical conditions and characterized. One of these identical samples was used for the studies described here. All measurements are performed in air at 295 K. The sample is maintained in a dark environment to suppress carrier photoexcitation in $SrTiO_3$ (bandgap ~ 3.2 eV). A set of electrodes, in contact with the interface and spaced $D_0 = 150$ μm apart, is fabricated using the techniques described in Ref. 9.

A conducting AFM tip, in contact with the top $LaAlO_3$ surface and biased at V_{tip} with respect to the interface, produces an interfacial metallic ($V_{tip}>0$) or insulating ($V_{tip}<0$) state directly below the area of contact. For the experiment described below, the gap between the conducting electrodes is first reduced to D=40 μm by "writing" (i.e., raster-scanning at V_{tip}=+10 V) two rectangular pads (Fig. 1A). The electric conductance between the two electrodes is monitored using a lock-in amplifier. The AFM tip, now biased at V_{tip} = +3 V, writes a line by scanning from one electrode to the

other. As the tip reaches the second electrode, a pronounced and abrupt conductance increase $\Delta G \approx 0.8$ nS is observed (Fig. 1B). This increase is not associated with any observed topographic changes of the structure, nor is it affected by subsequent imaging by an electrically isolated or grounded probe.

To provide a measure of the transverse dimension of the conducting wire, and to demonstrate that the writing process is reversible, the wire is subsequently "cut" with a reverse voltage $V_{tip} = -3$ V (Fig. 1C). As the AFM tip crosses the wire, the conductance decreases abruptly by $\Delta G \approx -0.8$ nS (Fig. 1D). Assuming the erasure process to have a resolution comparable to the writing process, the deconvolved differential profile $\left(d\sigma / dx\right)^{*-1}$ thus exhibits a full width at half maximum (FWHM) $\delta x = 3.3$ nm. Subsequent writing with positive voltages over the affected area (e.g., $V_{tip} = +3$ V) restores the conductance of the wire. The wire width depends sensitively on V_{tip}, increasing by three orders of magnitude as V_{tip} is raised from 3 V to 10 V. Test measurements were performed over a 24-hour interval and showed that the wires remain stable over that time frame.

The written wires are highly sensitive to externally applied electric fields. Fig. 2A shows the current-voltage (*I*-*V*) characteristics of a 20 μm long wire, created with $V_{tip} = 10$ V, that has been perturbed by the AFM probe with varying voltages. The AFM probe functions much like the gate of a ferroelectric field-effect transistor, except that the probe can be scanned. For each curve, the AFM probe is set to a voltage V_{gate} and scanned once across the wire. Afterwards, the in-plane current $I_{\parallel}$ is measured (using a picoammeter referenced to virtual ground) as a function of the voltage V_{sd} applied to one electrode. For low $\left|V_{gate}\right|$, the wire conductance is unaffected. However, as the tip bias becomes more negative, the wire becomes insulating and conducts only above a finite bias. This turn-on bias increases monotonically with $\left|V_{gate}\right|$. Eventually the *I*-*V*

curve becomes asymmetric, the likely origin of which is an asymmetry in the insulating barrier profile, produced by unequal electric fields on both sides of the AFM tip.

It is also possible to write isolated conducting islands or "dots" by applying voltage pulses $V_{tip}(t)$ with amplitude V_{pulse} and duration t_{pulse} to the tip while keeping the tip at a fixed position. During pulsed writing the two electrodes are grounded. The size of the dots depends on both V_{pulse} and t_{pulse}. For simplicity, we keep $V_{pulse} = 10$ V fixed and vary t_{pulse} to change the size of the dots. To determine the effective size of the dots, linear arrays of dots are created with various separations *d* (Fig. 3A). After writing the arrays, the ends of the arrays are contacted by writing conducting electrodes, which are separated by *D*=1 μm. As the contacts are being written, the conductance between the two electrodes is monitored using a lock-in amplifier. If the spacing between the dots is greater than the dot diameter, the dots will not overlap and no increase in conductance will be observed. Once the spacing becomes equal to or smaller than the dot diameter, the linear array will form a conducting wire, manifested as an abrupt increase in conductance between the two electrodes (ΔG), once the wire is attached. For each pulse duration, a sharp metal-insulator transition is observed as the dot spacing is reduced (Fig. 3B). The smallest non-conducting spacing $\underline{d_{nc}}$ and the largest conducting spacing $\overline{d_c}$ are plotted as a function of t_{pulse} (Fig. 3C). The critical spacing for conduction d_c is bound by these two measured quantities (i.e., $\underline{d_{nc}} > d_c \geq \overline{d_c}$) and scales linearly with pulse duration until pulse durations $t_{pulse} < 1$ ms are used. Below that threshold, the critical spacing levels off at $\overline{d_c} \sim 1$ nm.

The exceptionally small size of the features results from the nature of the writing process. Tunnelling measurements performed between the conducting AFM tip and the $LaAlO_3/SrTiO_3$ interface (Fig. 2B) show that for voltages $V_{tip} > V_t \sim 6$ V the current $I_\perp$ is governed by Fowler-Nordheim tunnelling between the tip and the interface. Tunnelling takes place over an area the radius of which may be estimated by assuming Hertzian

contact[21] to be $r_{contact} = 1.2$ nm. Writing at voltages smaller than V_t is possible, but not via direct tunnelling. Writing of conducting wires at, e.g., V_{tip}=3 V is only achieved if a conducting path already exists to one of the electrodes (e.g., Fig. 1). Isolated conducting regions cannot be written with $V_{tip}<V_t$.

Because there is no strong anisotropy present in the $SrTiO_3$ or $LaAlO_3$, the minimum lateral feature size is expected to be comparable to the scale for vertical confinement of the mobile electrons. Indeed, the smallest dot spacing observed is comparable to the observed thickness $\delta z = 2$ nm for the q-2DEG of a closely related system, $LaTiO_3/SrTiO_3$[1]. The lower-than-expected threshold for $\overline{d_c}$ may be the result of Anderson localization[22] within the quasi-one-dimensional conducting channel. Using $\delta x = \delta z = 2$ nm and l=1 μm, one obtains a resistivity for the wires $\rho = \delta x \delta z / \sigma l = 2 \times 10^{-3}\,\Omega$-cm, which is close to the Mott-Ioffe-Regel threshold.

We also performed similar experiments on bare $SrTiO_3$, 2uc $LaAlO_3$ on $SrTiO_3$ and 4uc $LaAlO_3$ on $SrTiO_3$, the details of which are described in the Supplemental Information. Experiments show that only in the sample with 3 uc $LaAlO_3$ layer thickness[9] conducting regions can be created and cleared at an insulating interface.

To provide insight into the electronic structure and stability of the metallic and insulating state of $LaAlO_3/SrTiO_3$, we performed first-principles Density Functional Theory (DFT) calculations of $LaAlO_3$ films on $SrTiO_3$ substrates. These calculations do not consider possible correlation effects at the interface[7,8]. Computational details are given in the Supplemental Information. Considering the experiment, an *n*-type (LaO/TiO_2) interface is used. The top surface of the $LaAlO_3$ is assumed to be clean and terminated with an AlO_2 layer. For 3 uc thick films, two structures are found to be stable. As shown in Fig. S 1, the two structures differ by the presence of oxygen vacancies on the surface. The two structures have dramatically different electrical

properties. The "ideal" film without vacancies (Fig. S 1A) is insulating. Removing oxygen ions from the $LaAlO_3$ surface layer (Fig. S 1B) accompanies the accumulation of mobile electrons at the interface.

The properties of the two stable structures can be understood by examining the local density of states (LDOS), shown in Fig. 4, and the schematic band diagrams derived from the LDOS (Fig. S 2). The ideal film has a strong electric field in the $LaAlO_3$, but at 3 uc the heterostructure is insulating. With one additional $LaAlO_3$ unit cell the system becomes metallic[9]. The strong field is energetically expensive and adding oxygen vacancies at the $LaAlO_3$ surface reduces and can compensate the electric field. Such $LaAlO_3$ oxygen vacancies contribute electrons to the conduction band, and the lowest energy conduction band states are in the $SrTiO_3$ (Fig. S 2A). At a density of n_V =1/4 vacancies per 1×1 surface cell, the formal charge of the surface has changed from -1e for the ideal AlO_2 surface to -1/2e for the $AlO_{1.75}$ surface. The 1/2 electron per unit cell populates the $SrTiO_3$ conduction band on the opposite side of the $LaAlO_3$ film. In this scenario, the oxygen vacancies in the $LaAlO_3$ and conduction electrons of the $SrTiO_3$ together cancel the field in the $LaAlO_3$, as seen in Fig. 4 and Fig. S 2B. The only metallic region in this system is the $SrTiO_3$ at the $LaAlO_3/SrTiO_3$ interface —the surface remains insulating.

In this model, switching between the two stable structures requires removing oxygen from the $n_V = 0$ surface and adding oxygen to the n_V=1/4 surface. There are likely significant kinetic barriers to these processes, which the charged AFM tip can overcome. Thus, without ruling out other mechanisms such as charging of trap states, this model suggests the possibility that a positively charged AFM tip "writes" metallic wires at the interface by removing oxygen from the $LaAlO_3$ surface, and a negatively charged AFM tip "erases" metallic regions by facilitating adsorption of oxygen or other anions. The ability to pattern reversibly high-mobility electron gases at nanoscale

dimensions provides new ground to develop devices for ultrahigh density information storage and processing. Integration with silicon-based devices is possible, as shown by reports of high-quality $SrTiO_3$/Si heterostructures produced by molecular-beam epitaxy[23].

Acknowledgement: We gratefully acknowledge helpful interactions and discussions with T. Kopp and S. K. Streiffer. Computations were performed at the DoD Major Shared Resource Centers. This work was supported by DARPA DAAD-19-01-1-0650, the DFG (SFB 484), the EC (Nanoxide) and the ESF (THIOX).

Correspondence and requests for materials should be addressed to J.L. (jlevy@pitt.edu).

1. Ohtomo, A., Muller, D. A., Grazul, J. L. & Hwang, H. Y. Artificial charge-modulation in atomic-scale perovskite titanate superlattices. *Nature* **419**, 378-380 (2002).
2. Ohtomo, A., & Hwang, H. Y. A high-mobility electron gas at the $LaAlO_3/SrTiO_3$ heterointerface. *Nature* **427**, 423-426 (2006).
3. Ohtomo, A. & Hwang, H. Y. Corrigendum: A high-mobility electron gas at the $LaAlO_3/SrTiO_3$ heterointerface. *Nature* **441**, 120-120 (2006).
4. Schneider, C. W., Thiel, S., Hammerl, G., Richter, C. & Mannhart, J. Microlithography of electron gases formed at interfaces in oxide heterostructures. *Appl. Phys. Lett.* **89**, 122101-3 (2006).
5. Huijben, M., Rijnders, G. et al. Electronically coupled complementary interfaces between perovskite band insulators. *Nat. Mater.* **5**, 556-560 (2006).
6. Hotta, Y., Susaki, T. & Hwang, H. Y. Polar Discontinuity Doping of the $LaVO_3/SrTiO_3$ Interface. http://arxiv.org/abs/0710.2174 (2007).
7. Okamoto, S., Millis, A. J. & Spaldin, N. A. Lattice relaxation in oxide heterostructures: $LaTiO_3/SrTiO_3$ superlattices. *Phys. Rev. Lett.* **97**, 056802-4 (2006).
8. Pentcheva, R. & Pickett, W. E. Charge localization or itineracy at $LaAlO_3/SrTiO_3$ interfaces: Hole polarons, oxygen vacancies, and mobile electrons. *Phys. Rev. B* **74**, 035112-7 (2006).
9. Thiel, S., Hammerl, G., Schmehl, A., Schneider, C. W. & Mannhart, J. Tunable quasi-two-dimensional electron gases in oxide heterostructures. *Science* **313**, 1942-1945 (2006).
10. Ahn, C. H., Triscone, J. M. & Mannhart, J. Electric field effect in correlated oxide systems. *Nature* **424**, 1015-1018 (2003).
11. Reyren, N. et al. Superconducting Interfaces Between Insulating Oxides *Science* **317**, 1196-1199 (2007).
12. Haeni, J. H. et al. Room-Temperature Ferroelectricity in Strained $SrTiO_3$. *Nature* **430**, 758-761 (2004).

13. Brinkman, A. et al. Magnetic effects at the interface between non-magnetic oxides. *Nat. Mater.* **6**, 493-496 (2007).
14. Helmolt, R. v., Wecker, J., Holzapfel, B., Schultz, L. & Samwer, K. Giant negative magnetoresistance in perovskitelike $La_{2/3}Ba_{1/3}MnO_x$ ferromagnetic films. *Phys. Rev. Lett.* **71**, 2331-2333 (1993).
15. Levi, B. G. Interface Between Nonmagnetic Insulators may be Ferromagnetic and Conducting. *Physics Today* **60**, 23-27 (2007).
16. Eckstein, J. N. Oxide interfaces: Watch out for the lack of oxygen. *Nat. Mater.* **6**, 473-474 (2007).
17. Schooley, J. F., Hosler, W. R. & Cohen, M. L. Superconductivity in Semiconducting $SrTiO_3$. *Phys. Rev. Lett.* **12**, 474-475 (1964).
18. Siemons, W. et al. Origin of charge density at $LaAlO_3$ on $SrTiO_3$ heterointerfaces: Possibility of intrinsic doping. *Phys. Rev. Lett.* **98**, 196802-4 (2007).
19. Kalabukhov, A. et al. Effect of oxygen vacancies in the $SrTiO_3$ substrate on the electrical properties of the $LaAlO_3/SrTiO_3$ interface. *Phys. Rev. B* **75**, 121404-4 (2007).
20. Herranz, G. et al. High Mobility in $LaAlO_3/SrTiO_3$ Heterostructures: Origin, Dimensionality, and Perspectives. *Phys. Rev. Lett.* **98**, 216803-4 (2007).
21. Frammelsberger, W., Benstetter, G., Kiely, J. & Stamp, R. C-AFM-based thickness determination of thin and ultra-thin SiO_2 films by use of different conductive-coated probe tips. *Applied Surface Science* **253**, 3615-3626 (2007).
22. Anderson, P. W. Absence of Diffusion in Certain Random Lattices. *Phys. Rev.* **109**, 1492-1505 (1958).
23. Li, H. et al. Two-dimensional growth of high-quality strontium titanate thin films on Si. *J. of App. Phys.* **93**, 4521-4525 (2003).
24. Perdew, J. P., Burke, K. & Ernzerhof, M. Generalized Gradient Approximation Made Simple. *Phys. Rev. Lett.* **77**, 3865-3868 (1996).
25. Kresse, G. & Furthmüller, J. Efficient iterative schemes for ab initio total-energy calculations using a plane-wave basis set. *Phys. Rev. B* **54**, 11169-11186 (1996).
26. Kresse, G. & Joubert, D. From ultrasoft pseudopotentials to the projector augmented-wave method. *Phys. Rev. B* **59**, 1758-1775 (1999).
27. Blöchl, P. E. Projector augmented-wave method. *Phys. Rev. B* **50**, 17953-17979 (1994).
28. Nakagawa, N., Hwang, H. Y. & Muller, D. A. Why some interfaces cannot be sharp. *Nat. Mater.* **5**, 204-209 (2006).
29. Jenkins, S. J. Ternary half-metallics and related binary compounds: Stoichiometry, surface states, and spin. *Phys. Rev. B* **70**, 245401-11 (2004).

Fig. 1 (A) Sketch of the experimental setup for writing a conducting wire. A voltage-biased AFM tip is scanned from one electrode toward a second one in contact mode. The tip generates an electric field that causes a metallic quasi-two-dimensional electron gas to form locally at the interface under the route of the tip. (B) Conductance between the two electrodes measured with a lock-in amplifier as a function of the tip position while writing a conducting wire with 3 V bias applied to the tip. A steep increase in conductance shows when the tip reaches the second electrode. (C) Sketch of the experimental setup for cutting a conducting wire. The negatively biased AFM tip moves in contact mode across the conducting wire. The tip erases the metallic q-2DEG locally when it crosses the conducting wire. The conductance between two electrodes is monitored as the tip scans over the wire. (D) Conductance between the two electrodes measured as a function of the tip position across the wire, while cutting the wire with the tip biased at -3 V. A sharp drop in conductance occurs when the tip passes the wire. The inset at right shows the conductance measured over the entire 8 μm scan length. The decrease in conductance can be fit to a profile $\sigma(x) = \sigma_0 - \sigma_1 \tanh(x/h)$ with best-fit parameters given by $\sigma_0 = 7.1\,\mathrm{nS}$, $\sigma_1 = 0.40\,\mathrm{nS}$ and $h = 2.9\,\mathrm{nm}$. Also plotted is the deconvolved differential conductance $(d\sigma/dx)^{*-1}$ showing a full width at half maximum $\delta x = 3.3\,\mathrm{nm}$.

Fig. 2. (A) Current $I_{\|}$ versus "source-drain" voltage V_{sd} of a 20 μm long q-2DEG wire with a potential barrier near the center, created with a negative "gate" bias V_{gate}. The barrier is created using the method shown in Fig. 1C. Different colors represent different tip biases. When the line is interrupted with a sufficiently large tip bias, the *I-V* characteristic becomes strongly nonlinear.

Conducting behavior is observed at large dc source voltages. (B) AFM tip current $I_{\perp}$ versus tip voltage V_{tip} with respect to grounded interface.

Fig. 3. (A) Schematic showing linear array of dots written with voltage pulses. (B) Conductance change as array is connected to electrodes, for various spacing between dots and different pulse durations. (C) Plot of minimum dot spacing for which the array is non-conducting $\underline{d_{nc}}$ and the maximum dot spacing for which the array is conducting $\overline{d_c}$, presented as a function of pulse duration t_{pulse}.

Fig. 4. Calculated local density of states for each layer in the 3 uc $LaAlO_3$ film and for the first 4 uc of the $SrTiO_3$ substrate. The solid blue curve corresponds to the "ideal" film, while the black curve corresponds to the film with surface oxygen vacancies. The ideal film is insulating and has a strong electric field in the $LaAlO_3$. With oxygen vacancies in the $LaAlO_3$ surface, the field is compensated, and 0.5 electrons per 1×1 unit cell enter the $SrTiO_3$ conduction states.

Fig. S 1. Stable structures of a 3 uc $LaAlO_3$ film on $SrTiO_3$. (A) Ideal film with no vacancies and (B) film with one surface oxygen vacancy per 2×2 unit cells. Dashed ovals indicate the row of oxygen atoms with the vacancy in the structure. The oxygen vacancies cause a significant rotation of the oxygen octahedra which propagates into the $SrTiO_3$.

Fig. S 2. Schematic band diagrams of $LaAlO_3/SrTiO_3$ heterostructures for ideal films without oxygen vacancies (left) and for films with oxygen vacancies (density n_V = 1/4, right). Computed energy differences are shown in large font. Experimental values (where known) are given in smaller font.

Fig. S 3. Computed energy gap between highest valence and lowest conduction states for ideal structures free of oxygen vacancies. The dashed line is a linear fit to the computed points. The dotted line shows the computed gap in bulk $SrTiO_3$.

Fig. S 4. Zero-temperature free energy of 3 uc $LaAlO_3$ films with surface oxygen vacancy densities of n_V = 0, 1/4, and 1/2. All energies have been shifted so $F(n_V=0)=0$.

Supplemental Information for *Nanoscale Control of an Interfacial Metal-Insulator Transition at Room Temperature*

C. Cen, S. Thiel, G. Hammerl, C.W. Schneider, K. E. Andersen, C. S. Hellberg, J. Mannhart, J. Levy

Experiments on samples with different $LaAlO_3$ layer thickness

Control experiments were performed on 4 uc $LaAlO_3/SrTiO_3$ and 2 uc $LaAlO_3/SrTiO_3$, and 0 uc $LaAlO_3/SrTiO_3$ (i.e., bare $SrTiO_3$) samples. Each of these samples was grown and contacted in a manner identical to that described for the 3 uc $LaAlO_3/SrTiO_3$ with the exception of the bare $SrTiO_3$, on which $LaAlO_3$ was not grown. A summary of our findings for all four samples (including 3 uc $LaAlO_3/SrTiO_3$) is contained in Table 1.

Photosensitivity: The conductance of the 3 uc $LaAlO_3/SrTiO_3$ sample is highly sensitive to light above the bandgap of $SrTiO_3$ (~3.2 eV), exhibiting persistent photoconductivity that decays over ~12-24 hrs after being stored in a dark environment. The 4 uc sample showed a similar photosensitivity; however the 2 uc and 0 uc sample did not exhibit photosensitive behaviour.

Background conductance: The 0 uc, 2 uc and 3 uc sample exhibited a very small background conductance of several nS, while the 4 uc sample showed a much larger background conductance (~1200 nS).

Writing conducting regions: Two methods of writing were demonstrated with the 3 uc sample: (1) writing of isolated structures that are later contacted, and (2) writing of structures beginning from one or both electrodes. For the 4 uc sample, the large conductance of the interface can be further increased by writing (using either method),

although the voltage threshold for writing is higher compared to the 3 uc sample. Isolated conducting structures could not be written on either the 2 uc or the 0 uc sample. Attempts to write conducting lines beginning from one of the electrodes and ending at the other were unsuccessful in that any resulting conductance change coincided with highly visible damage to the sample surface, taking the form of a 1-2 nm protruding line that follows the path taken by the AFM tip. Note that writing for the 3 uc or 4 uc samples did not produce any observable topographic changes.

Erasing conducting regions: In 3 uc sample, conducting regions became insulating after erased by applying a reverse voltage (-10 V); however, in 4 uc sample, only the conductance change induced by writing was able to be reversed after several erase attempts, the interface remained conducting regardless of the bias applied.

$LaAlO_3$ layer thickness	**0 uc**	**2 uc**	**3 uc**	**4 uc**
Photosensitive?	No	No	Yes	Yes
Background conductance	<10 nS	<10 nS	<10 nS	>1 μS
Write isolated structure?	No	No	Yes	Yes*
Write connected structure?	Not possible without producing damage	Not possible without producing damage	Possible for V_{tip}>3 V	Possible* for V_{tip}>7 V
Topography change after writing	Yes	Yes	No	No
Cut with V_{tip}=-10 V	NA	NA	Yes	Yes*, after several attempts

* For the 4 uc sample, writing and cutting procedures only modulate the conductivity. The interface is always conducting.

Table 1. Summary of findings for four $LaAlO_3/SrTiO_3$ samples investigated.

First-Principles Calculations

We performed first-principles density functional calculations of $LaAlO_3$ films on a $SrTiO_3$ substrate using the generalized-gradient approximation (GGA) [24] and projector-augmented wave functions as implemented in VASP [25-27]. For the calculations of the energy gap in the ideal films, a sandwich geometry was used with identical $LaAlO_3$ films on each side of a 9.5 monolayer (ML) $SrTiO_3$ slab (9 SrO layers and 10 TiO_2 layers). For the calculations to determine the structure and stability of oxygen vacancies, a 5.5 ML $SrTiO_3$ slab was used, terminated on the bottom with 1 ML $LaAlO_3$. In all calculations, a vacuum region of at least 0.8 nm between repeated slabs was used. The in-plane lattice constant was held fixed at the computed lattice constant of bulk $SrTiO_3$, $a_{SrTiO_3} = 0.3948$ nm . A cutoff of 282.8 eV was used for the planewave basis. For the insulating systems, 6×6 Monkhorst-Pack (MP) sampling of the Brillouin zone per 1×1 unit cell was used. For the metallic systems, 12×12 MP sampling and Fermi smearing of 0.03 eV was used. Forces were converged to less than 110 meV/nm.

Fig. S 3 shows the energy gap between the highest valence and lowest conduction states. The gap decreases linearly with film thickness. At 4 ML, the gap becomes negative (taken between M and Γ), and two metallic regions form in the system: an electron gas in the $SrTiO_3$ and a hole gas at the surface of the $LaAlO_3$. Thiel et al. also find that the metal-insulator transition occurs between 3 and 4 uc.

The metal-insulator transition in the ideal film is caused by the polar catastrophe– the electric potential across the $LaAlO_3$ increases with thickness. When it exceeds the band gap, electrons move from the surface valence states to the $SrTiO_3$ conduction states [28].

To determine the stability of oxygen vacancies, we must first determine the possible range of the oxygen chemical potential μ_O [29]. This chemical potential is

bounded from above by the chemical potential of the triplet O_2 molecule, $\mu_O < \mu_{O_2}/2 = -4.917$ eV .

The three chemical potentials must obey the constraint $\mu_{La} + \mu_{Al} + 3\mu_O = \mu_{LaAlO_3}^{bulk} = -40.168$ eV . The chemical potentials of La and Al have inequality constrains which must be satisfied to avoid phase segregation:

$\mu_{La} < \mu_{La}^{bulk} = -7.916$ eV , and $\mu_{Al} < \mu_{Al}^{bulk} = -3.749$ eV .

Thus the allowable range of μ_O is $-9.501\,\text{eV} \le \mu_O \le -4.917$ eV .

To determine the stability of surface oxygen vacancies in the 3 uc films, we show in Fig. S 4 the free energy of films with three different oxygen vacancy densities. The free energy F is constructed as $F = E - n_{La}\mu_{La} - n_{Al}\mu_{Al} - n_O\mu_O$, where E is the total energy of the system, n_i are the numbers of La, Al, and O atoms, and the μ_i are the respective chemical potentials. We see in Fig. S 4 that both the ideal system with no vacancies ($n_V = 0$) and the $n_V = 1/4$ systems are stable over a range of allowed oxygen chemical potentials, while $n_V = 1/2$ is never stable. We expect that a range of vacancy densities (EQ) may be stable. All systems with $n_V > 0$ have metallic interfaces. The $n_V = 1/4$ system required a rather large 2×2 computational cell; investigating smaller vacancy densities will require even larger cells.

GGA+*U* calculations were also performed to test the robustness of these results against correlation effects represented by a Hubbard *U*. Both films, with and without an oxygen vacancy, were relaxed using the GGA+*U* formalism with $U = 4$ eV and $J = 1$ eV applied to the Ti *d*-states at the interface. These spin-polarized calculations were performed using an 8×8 *k*-point grid within the 1×1 surface unit cell. Negligible changes were found for the free energy, the structure, and the local density of states, providing confidence that GGA alone sufficiently describes these films.

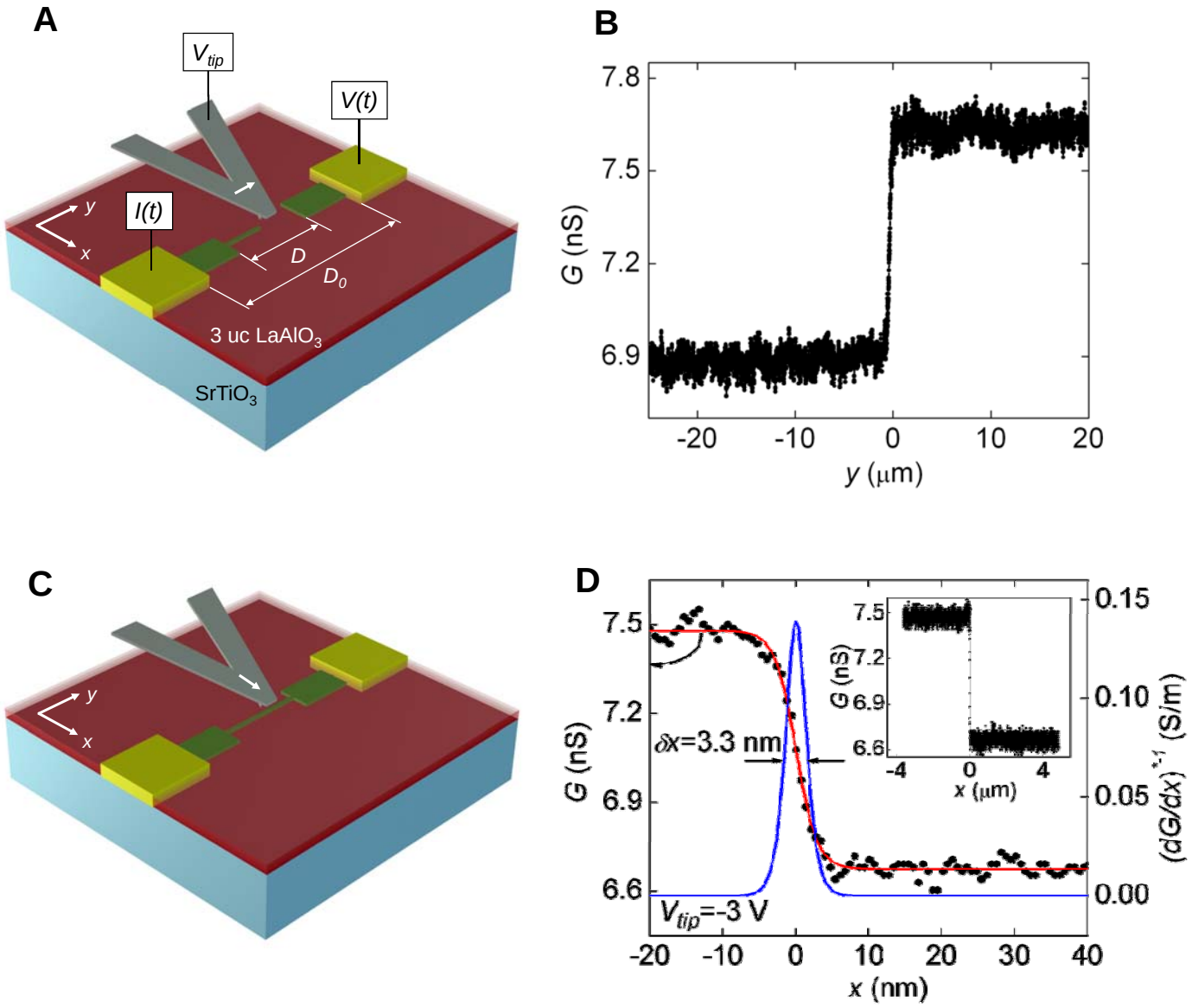

Cen et al., Fig. 1

A

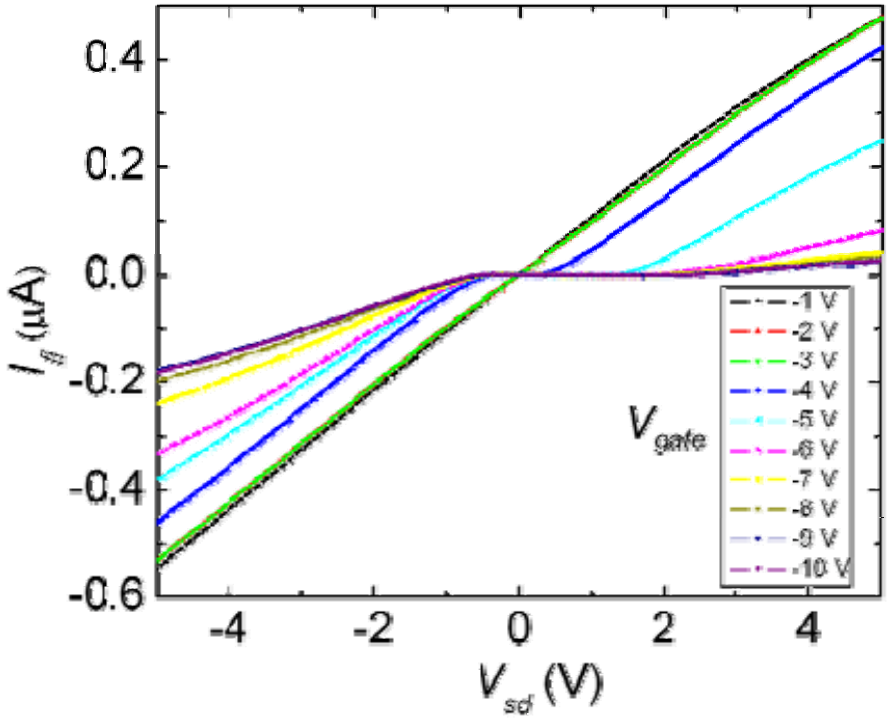

B

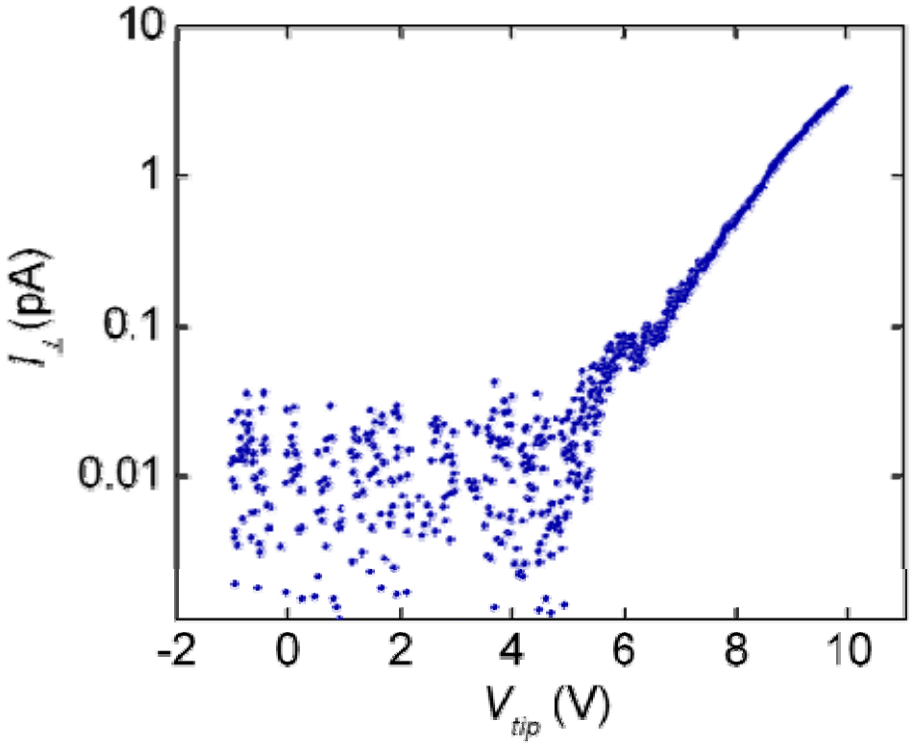

Cen et al., Fig. 2

A

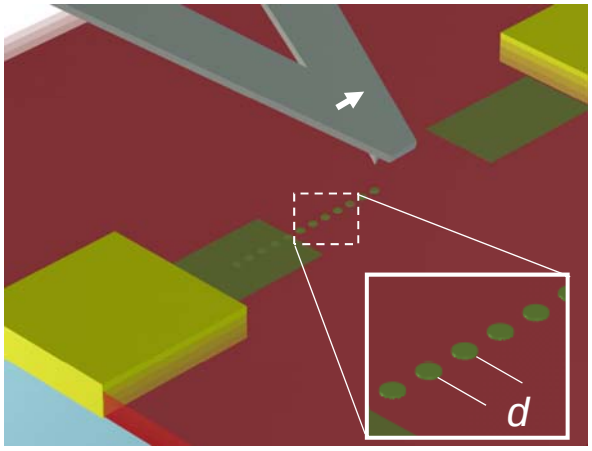

B

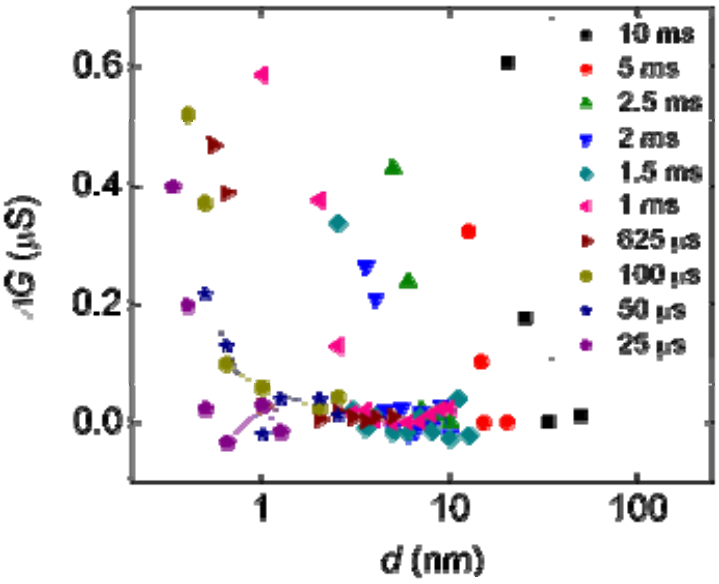

C

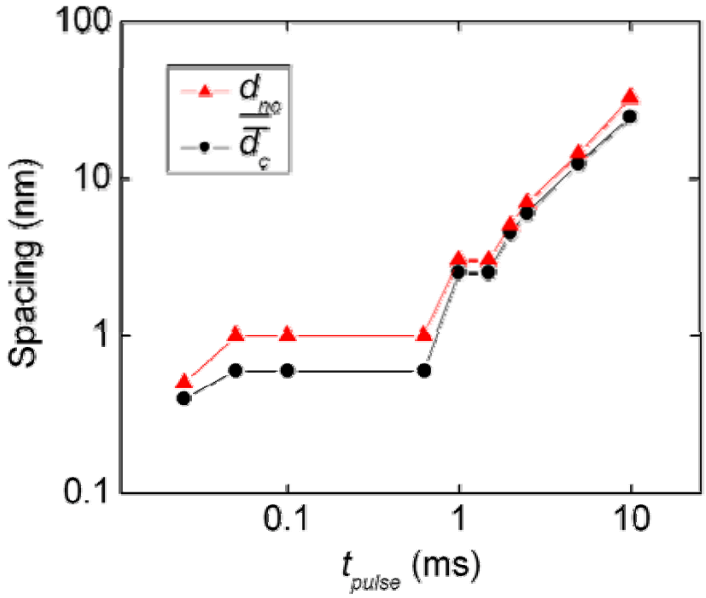

Cen et al., Fig. 3

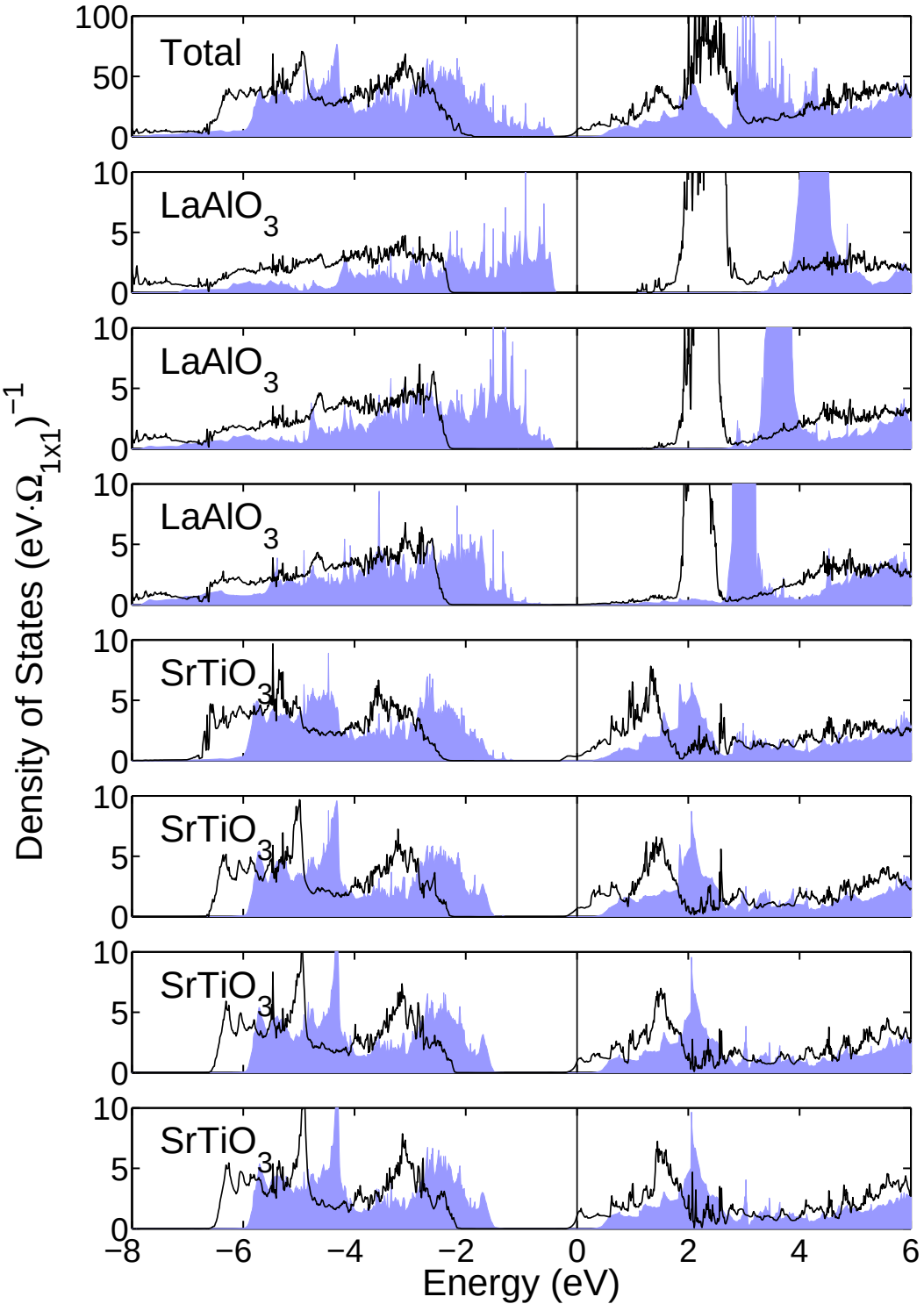

Cen et al., Fig. 4

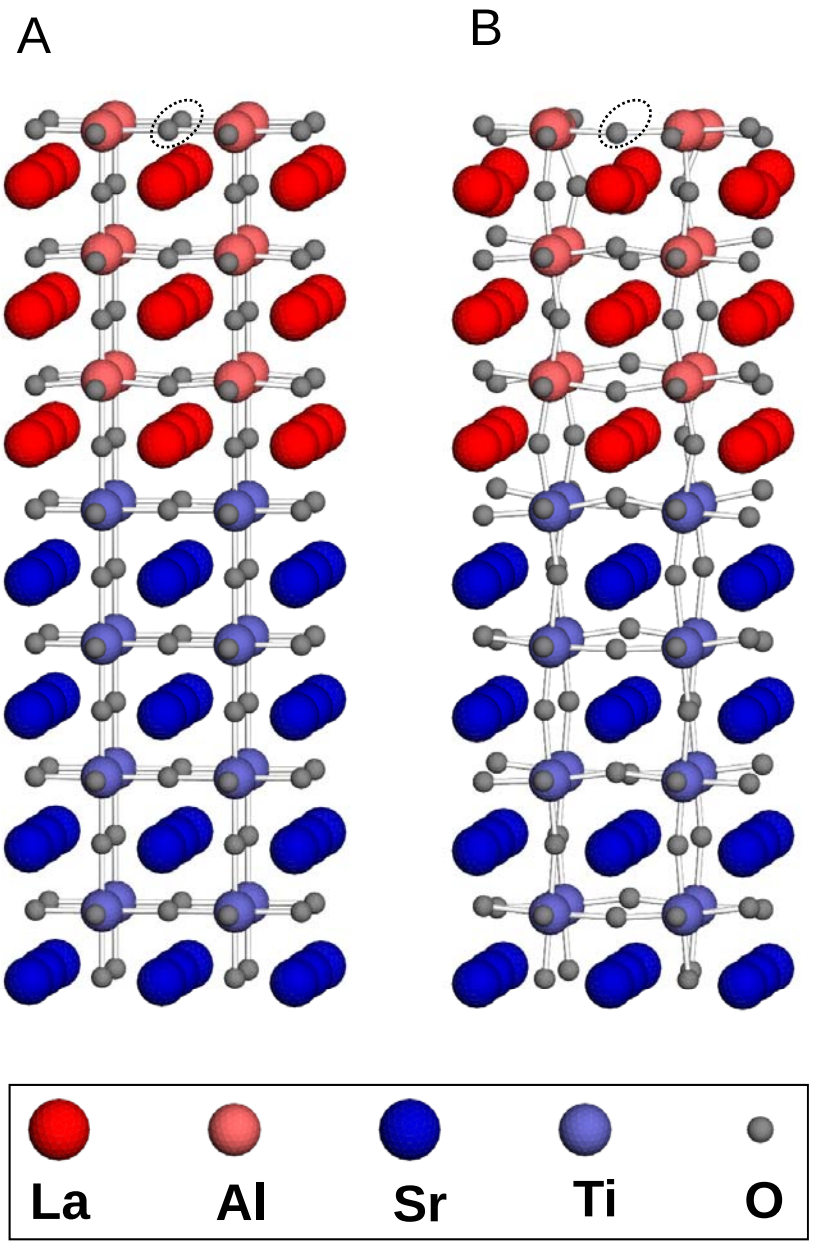

Cen et al., Fig. S1

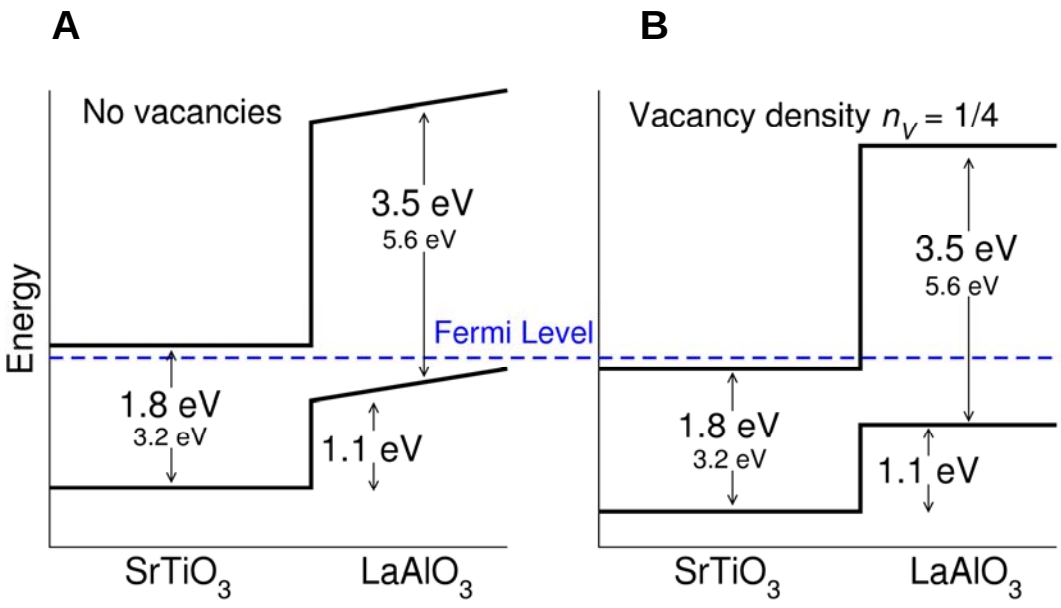

Cen et al., Fig. S2

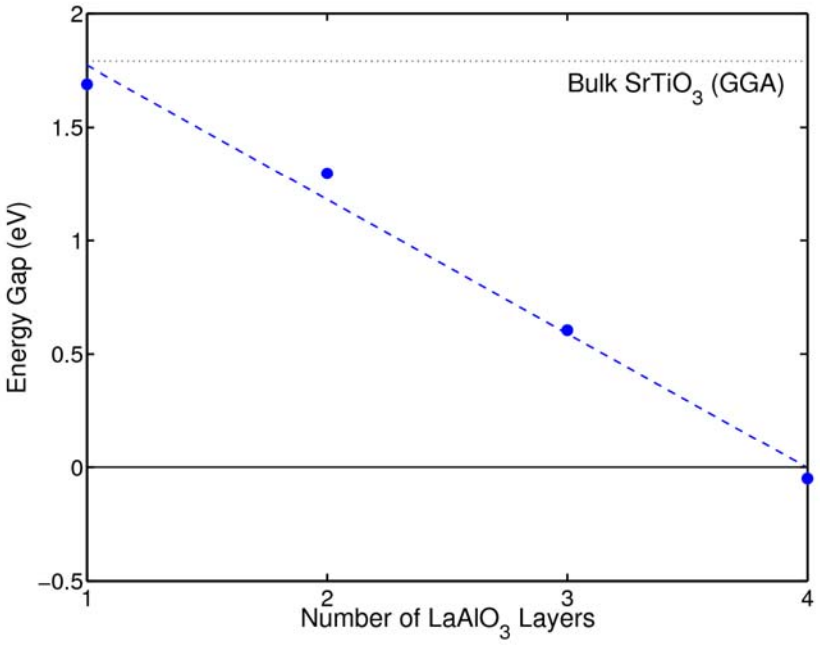

Cen et al., Fig. S3

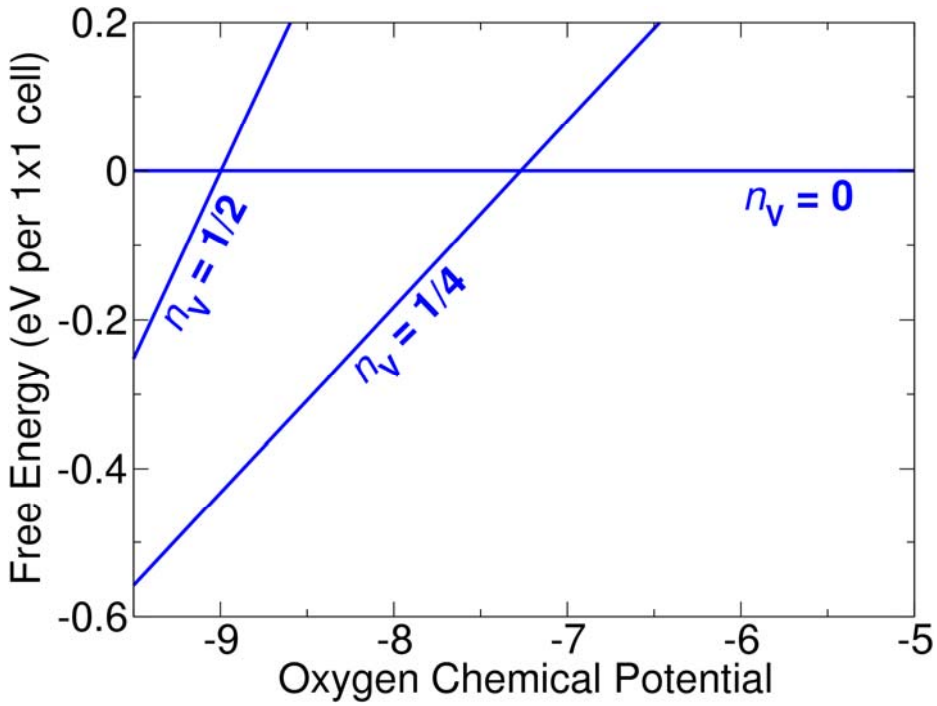

Cen et al., Fig. S4